Check for updates

High resolution 3D visualization of the spinal cord in a post-mortem murine model

INNA BUKREEVA,[1,2,*] VICTOR ASADCHIKOV,[3] ALEXEY BUZMAKOV,[3] MARINA CHUKALINA,[3,4] ANASTASYA INGACHEVA,[4] NIKOLAY A. KOROLEV,[5] ALBERTO BRAVIN,[6] ALBERTO MITTONE,[7] GABRIELE E. M. BIELLA,[8] ALEJANDRA SIERRA,[9] FRANCESCO BRUN,[10] LORENZO MASSIMI,[11] MICHELA FRATINI,[1,12] AND ALESSIA CEDOLA[1]

[1]*Institute of Nanotechnology- CNR, Rome Unit, Piazzale Aldo Moro 5, Italy*
[2]*P. N. Lebedev Physical Institute, RAS, Leninsky pr., 53, Moscow, Russia*
[3]*Shubnikov Institute of Crystallography FSRC "Crystallography and Photonics" RAS, Leninsky prosp., 59, Moscow, Russia*
[4]*Intitute for Information Transmission Problems RAS, Bolshoi Karetny per, 9, Moscow, Russia*
[5]*National Research Nuclear University /Moscow Engineering Physics Institute, Kashirskoye Highway, 31 Moscow, Russia*
[6]*European Synchrotron Radiation Facility, 71 Avenue des Martyrs, Grenoble, France*
[7]*CELLS - ALBA Synchrotron Light Source, Carrer de la Llum, 2-26, Cerdanyola del Valles, Barcelona, Spain*
[8]*IBFM-CNR, Via Fratelli Cervi, 93 - 20090 Segrate-Milan, Italy*
[9]*Biomedical Imaging Unit, A.I. Virtanen Institute for Molecular Sciences, University of Eastern Finland, Kuopio, Finland*
[10]*Department of Engineering and Architecture, University of Trieste, Via A. Valerio, 6/1 Trieste, Italy*
[11]*Department of Medical Physics and Biomedical Engineering, University College London, Gower Street, London, WC1E 6BT, United Kingdom*
[12]*Fondazione Santa Lucia I.R.C.C.S., Via Ardeatina 306, Roma, Italy*
[*]inna.bukreeva@cnr.it

Abstract: A crucial issue in the development of therapies to treat pathologies of the central nervous system is represented by the availability of non-invasive methods to study the three-dimensional morphology of spinal cord, with a resolution able to characterize its complex vascular and neuronal organization. X-ray phase contrast micro-tomography enables a high-quality, 3D visualization of both the vascular and neuronal network simultaneously without the need of contrast agents, destructive sample preparations or sectioning. Until now, high resolution investigations of the post-mortem spinal cord in murine models have mostly been performed in spinal cords removed from the spinal canal. We present here post-mortem phase contrast micro-tomography images reconstructed using advanced computational tools to obtain high-resolution and high-contrast 3D images of the fixed spinal cord without removing the bones and preserving the richness of micro-details available when measuring exposed spinal cords. We believe that it represents a significant step toward the in-vivo application.

1. Introduction

The spinal cord (SC) is exposed to a wide variety of diseases. In particular, the incidence of spinal cord injuries in the world is about 40-80 new cases per year per million inhabitants [1], corresponding to 250,000-500,000 new cases per year of people suffering from traumatic and non-traumatic spinal cord injuries. The non-traumatic injuries are due to neuroinflammation and neurodegeneration of the spinal cord. In this context, it emerges the need of identifying

and introducing non-invasive methods, with the ability to investigate the spinal cord anatomical conditions at a spatial resolution allowing the evaluation and the optimization of pharmacological or rehabilitation treatments.

A variety of imaging techniques such as magnetic resonance imaging (MRI), ultrasound, positron emission tomography (PET) and X-ray computed tomography (CT) are in daily use for the investigation of the spinal cord. However, the high-resolution 3D visualization of intact spinal cord in the vertebral canal is a challenging aim for these techniques. Indeed, the dense material composing the vertebrae surrounding the spinal cord scatters and attenuates the signal, thus making some imaging techniques inefficient without invasive procedures including the complete, or at least partial, removal of the vertebral bone [2–4]. Magnetic resonance and X-ray computed tomography imaging are well established techniques applied to SC preclinical studies. Magnetic resonance imaging at a microscopic level (micro-MRI) non-invasively penetrates the bones and yields reasonably well-resolved 3D images of the spinal cord inside the spinal canal [5]. However, the spatial resolution and contrast of micro-MRI are insufficient to reveal the SC neuronal and vascular networks [6]. X-ray micro-computed tomography (micro-CT) imaging has a noticeable advantage in the depth-to-resolution ratio with respect to other imaging techniques. It permits in fact to visualize large tissue volumes (up to the whole organ) at high spatial resolution (5–50 μm to 100 nm) [7–9] and high contrast between different absorbing tissues [10]. The technique has been used with great success in post-mortem and in-vivo small animal models [7,10–12]. Micro-CT is a relevant tool for imaging highly absorbing mineralized structures, such as bone [11,13], and soft tissue after administration of X-ray-absorbing contrast agents [14,15]. Combined with angiography contrast agents, micro-CT has been widely used in the investigation of vascularization and angiogenesis in different organs, including the brain and the spinal cord [16,17]. The main drawback of micro-CT is the poor contrast resolution of soft tissues when applied without invasive contrast agents [10].

X-ray Phase Contrast micro-Tomography (micro-XPCT), based on the phase modulation induced by a sample in a coherent or partially coherent X-ray beam, is highly sensitive to small density variations in weakly absorbing materials, without the need of exogenous contrast agents. Different X-ray phase imaging techniques such as analyzer-based imaging [18], propagation-based imaging (PBI) [19,20], crystal interferometry [21], grating-based [22] and edge illumination imaging [23], have been developed and several of them have been demonstrated to be compatible with the high resolution 3D imaging of large biological samples. However, some imaging techniques requiring additional X-ray optical elements have limit in the spatial resolution above several micron due to a fabrication issue. The PBI has received a great interest due to the simple optics-less set-up exploiting only X-ray propagation in free space and achievable spatial resolution of micron level with large field of view. Moreover, single-distance PBI significantly reduces the acquisition time compare with other imaging techniques. Recently, the macro- and micro-morphology of post-mortem entire mice spinal cords, including the complex organization of their vascular and neuronal networks, has been successfully imaged in Refs. [24–26]. However, despite the great potential of micro-XPCT, until now the attainment of high-resolution, contrast agent-free 3D images of the SC microvascular and neuronal networks has been done only in the case of exposed spinal cords fully removed from the vertebral column [25,26]. Clearly, this has limited the application of the method to post-mortem measurements. Another critical issue for in-vivo models is radiation tolerance, which at the moment sets a limit to the obtainable resolution in computed tomography down to a few tens of micron for living animals [27,28].

In this work, we present the potentiality of the micro-XPCT to obtain high-resolution and high-contrast 3D images of post-mortem fixed mouse SC without the need to extract the SC from the vertebral canal. Moreover, by exploiting a suitable computational platform, we demonstrated that micro-XPCT with sparse set of tomographic projections and, therefore, a reduced delivered dose on the sample, preserves details typically achievable when the exposed spinal cord is

imaged. Our findings constitute, as a whole, an important step towards the implementation of the micro-XPCT technique for future central nervous system (CNS) analysis in-vivo.

2. Results

The main goal of our research was to attain high-resolution, contrast agent-free 3D images of the intact post-mortem murine SC inside the spinal column. We analysed three different types of specimens: samples A were prepared without contrast agent, while sample B and sample C were injected with Iodixanol and Microfil NW-130 contrast agents, respectively. Samples B&C were perfused with radio-opaque agents to validate the SC microvasculature. The images were acquired during XPCT imaging experiments at the synchrotron beamlines ID17 (ESRF, France) and TOMCAT (PSI, Switzerland). Different experimental parameters (e.g. beam energy and pixel size, see Table 1) were adopted in order to increase the visibility of different features (e.g. spinal cord grey matter and white matter, the vascular network etc.) in 3D images of the SC. The summary of experimental parameters is given in the Table 1 and in the Materials and methods section.

Table 1. Experimental parameters used to the imaging of the presented samples.

Setup	Sample	Contrast agent	Energy (keV)	Pixel size ($micron^2$)	Distance Sample/detector (m)
ESRF ID17	Sample A	saline solution	30	3.50×3.50	2.30
ESRF ID17	Sample A	saline solution	60	3.50×3.50	2.30
ESRF ID17	Sample B	Iodixanol	60	3.50×3.50	2.30
ESRF ID17	Sample B	Iodixanol	60	1.00×1.00	0.60
PSI TOMCAT	Sample A	saline solution	24	0.64×0.64	0.05
PSI TOMCAT	Sample A	saline solution	24	1.60×1.60	0.21
PSI TOMCAT	Sample C	Microfil	24	1.60×1.60	0.21

During the step-scan tomography image acquisition, data were taken at a fixed sample-to-detector distance. Starting from the acquired intensity map we obtained the image of the object by retrieving the phase map by using the Paganin's method extended for multi-materials [29–33]; subsequently, the retrieved images were used for volume reconstruction. Tomographic reconstruction was performed using the conventional Filtered-Back-Projection (FBP) algorithm and the advanced Simultaneous Iterative Reconstruction Technique (SIRT) [34,35] with Total Variation regularization [36,37]. We applied the FBP algorithm to the full set of angular projections evenly spaced over the 180 degrees rotation angle (2000 and 1601 projections in Figs. 1–2 and in Figs. 3–5, respectively) to obtain the 3D image of the spine and spinal cord preserving the richness of micro-details (see Figs. 1–5). The application of FBP to sparse projections data led instead to a complete loss of information while the regSIRT [38,39] method allowed keeping the morphological information (the results for Sample A are reported in Fig. 6).

2.1. ESRF ID17 experiment

Figure 1(a,b) shows 3D axial views of the reconstructed lumbar part of the SC with the vertebrae (sample A) measured at 60 keV in the ESRF ID17 experiment. This figure reports the average intensity through a slab of 50 slices (the image processing procedures were performed using the open source ImageJ/Fiji [40] tools). Figures 1(a), 1(b) show two different spinal cord regions of the Sample A measured at a sample-detector distance of 2.3 m using a detector pixel size of 3.5 micron. High energy and relatively low resolution put in evidence only the structure of the highly absorbing backbone and the features comparable with vascularization in the tissue surrounding the spinal cord, while the low absorbing soft tissue of the spinal cord inside the spinal canal gave only some morphological information such as the shape of the SC.
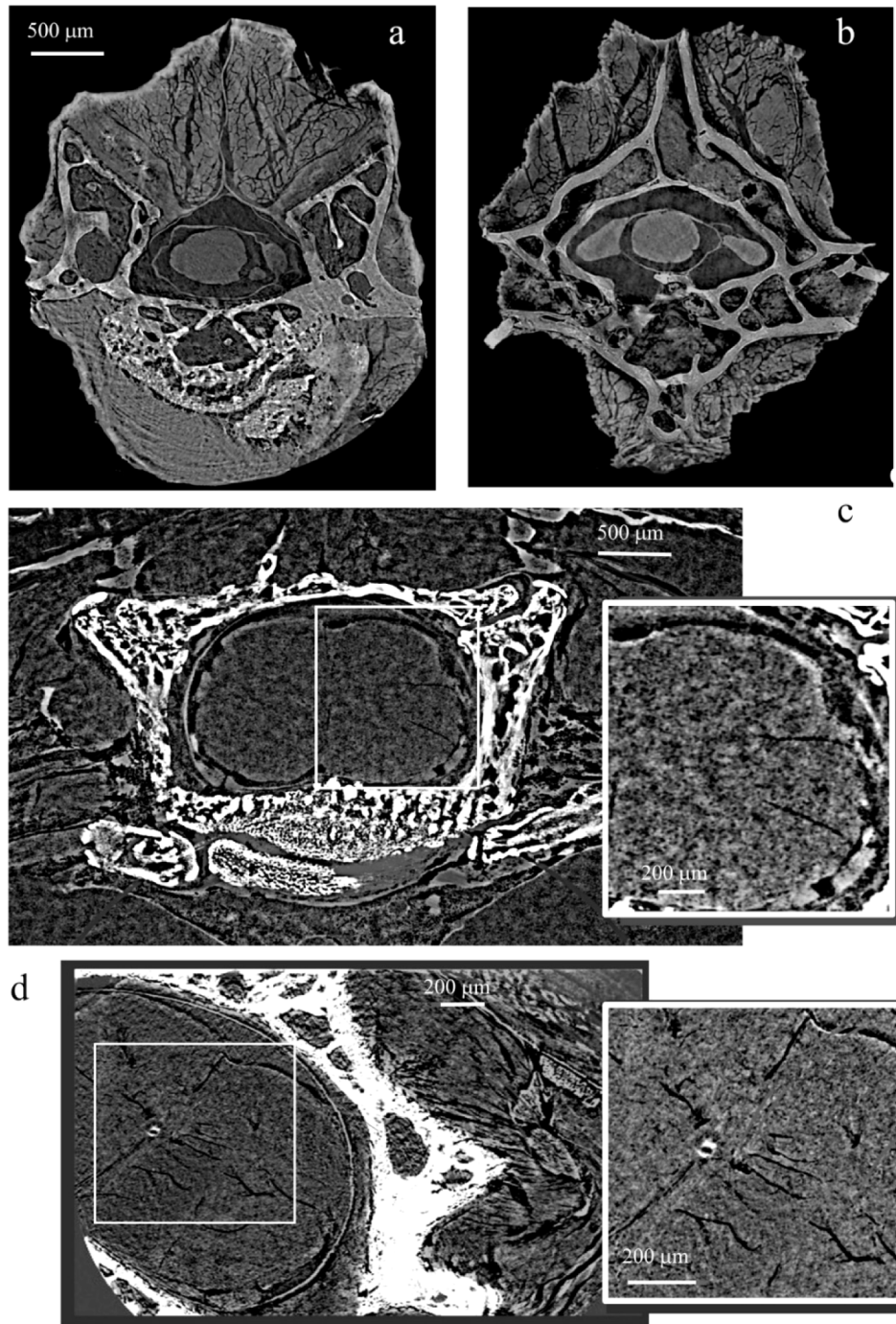
Fig. 1. Micro-XPCT reconstruction of the *murine* spinal cord (axial view) recorded at 60 keV: (a-b) unstained sample (sample A, lumbar part of spine), pixel size of 3.5 micron, sample-detector distance 2.3 m, (c) sample B (cervical part of spine) perfused with iodine contrast agent, pixel size of 3.5 micron and the sample-detector distance 2.3 m, (d) sample is the same as in Fig. 1(c), pixel size of 1 micron, sample-detector distance 0.6 m. A 50 slices volume of the sample is presented in the figure. ESRF ID17 beamline experiment. The number of tomographic projections was equal to 2000.

The perfusion of the sample with iodine (sample B) provided some additional details on the vascularization, as it can be seen in Fig. 1(c) showing the cervical part of spine. However, the features of vascular and neuronal networks cannot be distinguished with a pixel size of 3.5 micron. With an increased spatial resolution (pixel size of 1 micron) and with the corresponding adjustment of the sample-detector distance to 0.60 m, the details of the stained vascular network (segmented in black) in Sample B clearly appear together with the central canal, as reported in Fig. 1(d). However, the details of white/grey matter and the micro-morphology of the SC soft tissue, in particular neuronal network, remain invisible.

By decreasing the incident energy from 60 keV to 30 keV we obtained additional details in the soft tissue image, without using any contrast agent (sample A) at a relatively low spatial resolution (pixel size of about 3.5 micron). Figure 2(a) is the average intensity through 50 slices and it shows the axial view of the sample A (the cervical part of spine). The typical H-shape of the spinal cord starts to be visible. In addition, the meninges (blue arrows) are discernible. Figure 2(b) is the SC area tagged in Fig. 2(a) with a rectangular frame. It was obtained through the maximum intensity over 50 slices, which allowed us to better distinguish the morphology and microarchitecture of the organ.
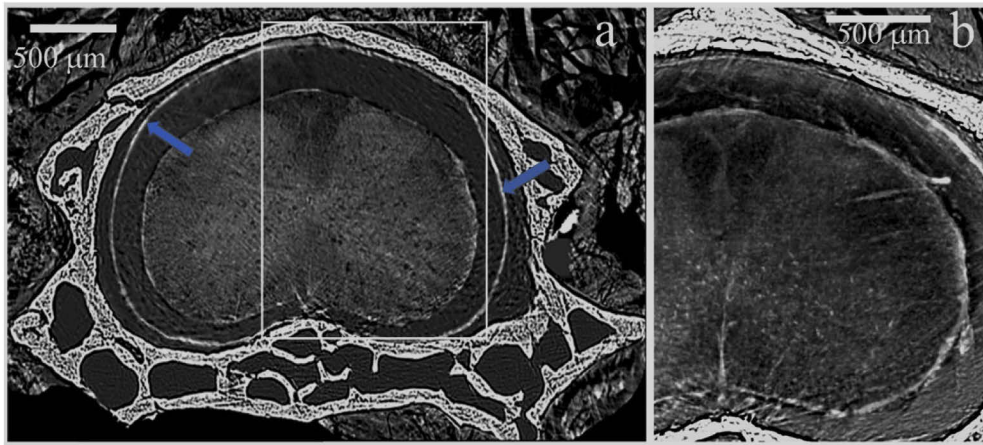

Fig. 2. (a) Micro-XPCT reconstruction of the vertebrae and spinal cord of the sample A (the cervical part of spine), axial view. Average intensity Z-projection through 50 slices; (b) zoom of the area tagged in Fig. 2(a) with the rectangular frame. Maximum intensity Z-projection through 50 slices. ESRF ID17 beamline experiment. The image was obtained from projections acquired at 30 keV, pixel size of 3.5 micron and the sample-detector distance 2.3 m; the number of tomographic projections was equal to 2000.

2.2. PSI TOMCAT experiment

In the experiment at PSI TOMCAT beamline with incident energy 24 keV, pixel size of 1.6 micron and corresponding adjustment of the sample-detector distance to 0.21 m, we obtained a detailed image of the healthy spinal cord with vertebral canal of the sample A (the cervical part of spine), as it can be seen in Fig. 3(a). The Nissl-stained histological section in Fig. 3(c) shows the shape and details of the white-grey matter interfaces of the spinal cord, which is in a good agreement with the tomographic data.

Figure 4 reports a virtually selected region of interest including the SC (axial view of the cervical part). In this case, even without contrast agent, the features comparable with vascularization, the nerve fibers and cells can be clearly seen as demonstrated by the comparison with the histology. Figures 4(a) and 4(f) show the tomographic reconstruction of the sample with a pixel size
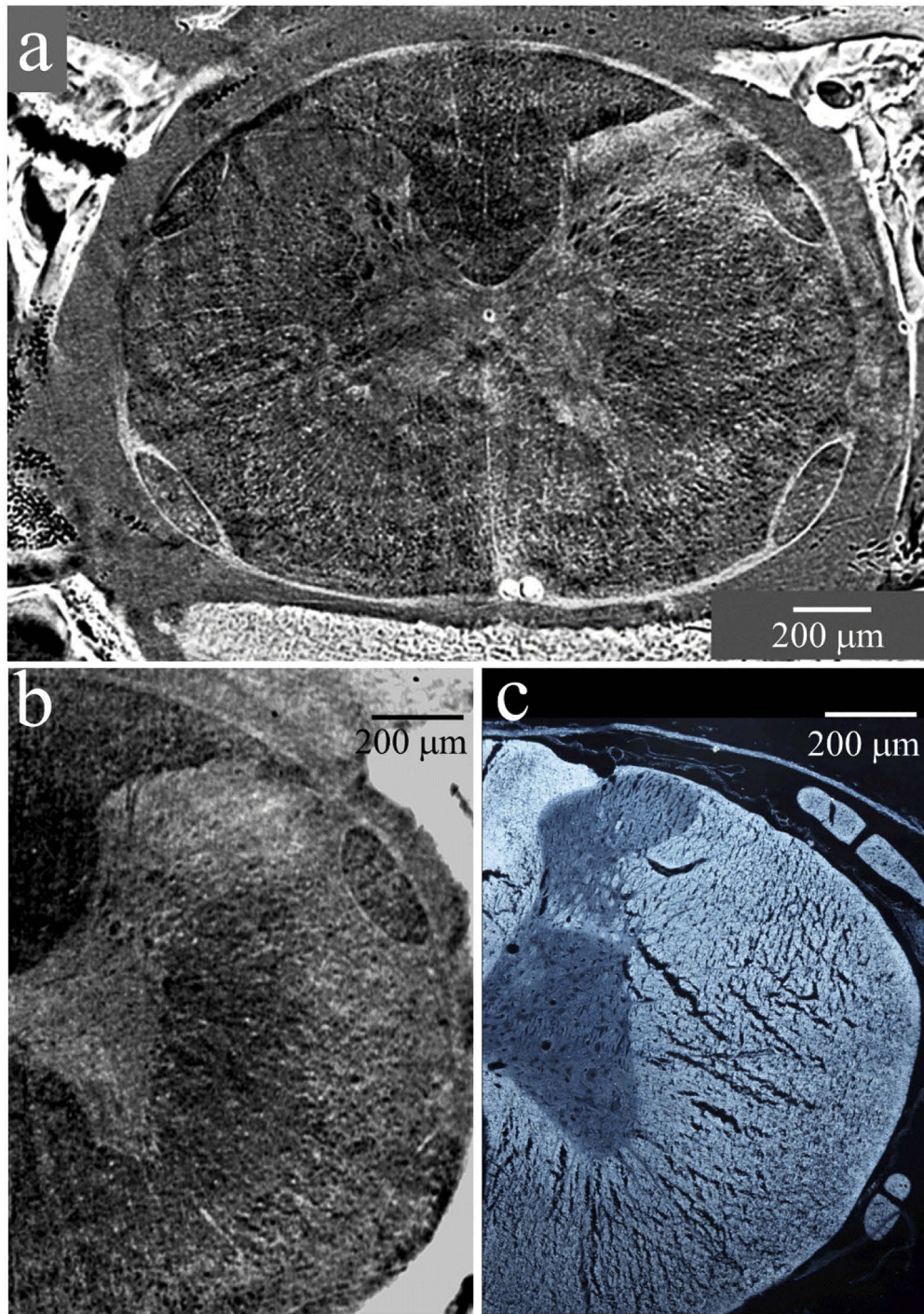
Fig. 3. (a) Micro-XPCT reconstruction of 50 slices volume (average intensity Z-projection) of the sample A (the cervical part of spine). (b) average intensity Z-projection through a 10 micron thick slab; (c) histological slice with Nissl staining (dark field) of the same area in (b). (a-b) PSI TOMCAT beamline experiment. The projections were acquired at 24 keV, sample-detector distance 0.21 m, pixel size of 1.6 micron; the number of tomographic projections was equal to 1601.
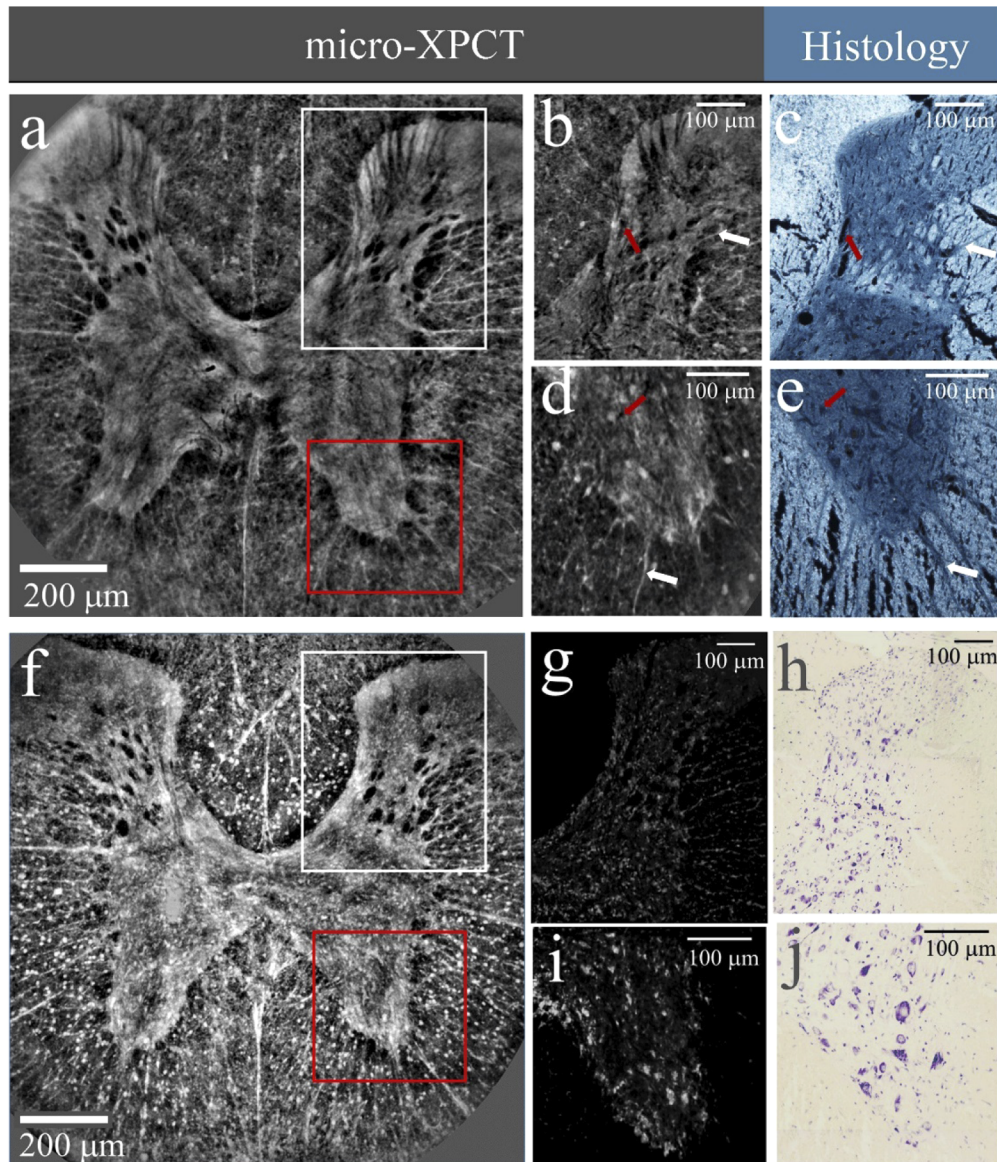
Fig. 4. (a) The tomographic image of the spinal cord of the sample A, the same as shown in Fig. 3, (average intensity Z-projection through a 30 micron thick slab). The details, at the white/grey matter interface show features comparable with the micro-vascularization and nerve fibers in the ventral (b) and in the dorsal horns (d). The areas with the ventral and the dorsal horns are shown in (a) with white and red rectangular frames correspondently. Dark field photomicrographs of Nissl-stained 10 micron thick section of the ventral (c) and dorsal horns (e). Red and white arrows are pointed at features comparable with blood vessels and nervous fibers, respectively. (f) Axial view of the spinal cord. Maximum intensity Z-projection through a 30 micron thick slab. The details in a 10 micron thick section show cells in ventral (g) and in the dorsal horns (i) visualized after segmentation. The areas corresponding to the ventral and the dorsal horns are shown in (f) with white and red rectangular frames correspondently. Bright field photomicrographs of Nissl-stained sections of the ventral horn (h) and dorsal horn (j). (a, b, d, f, g, i) PSI TOMCAT beamline experiment. The images were obtained using 24 keV X-rays, sample-detector distance 0.05 m, pixel size of 0.64 micron, the number of tomographic projections was equal to 1601; (c,e,h,j) histological sections.

reduced down to 0.64 micron and at sample-detector distance 0.05 m ((a) average intensity and (f) maximum intensity through a slab of 30 micron). The images in Figs. 4(b,d) are 10 micron thick sections (average intensity) of the ventral horn (white frame) and of the dorsal horn (red frame) of Fig. 4(a). We compared them with histological photomicrographs reported in Fig. 4(c,e). For visualization purposes we imaged the Nissl-stained sections in the dark-field contrast, where the vascularization appears black due to the lack of tissue, and by extension, staining. Figures 4(g,i) are 10 micron-thick sections (maximum intensity) of the ventral (white frame) and the dorsal horns (red frame) of Fig. 4(f). The bright spots in Fig. 4(g,i) represent the neuronal cells, as clearly identified also in the Nissl slices in Fig. 4(h,j).

Figures 5 reports the results of sample C (the cervical part of SP previously injected with Microfil). Figures 5(a-c) show the 3D rendering of the micro-XPCT reconstructed sample with a voxel size of $1.6 \times 1.6 \times 1.6 \ \mu m^3$. The sketch of the spine shown in Fig. 5(d) explains the orientation of the sample. In Fig. 5(c), outside the backbone, the ascending vertebral arteries partially filled by the contrast agent are clearly seen (marked with red arrow). Both
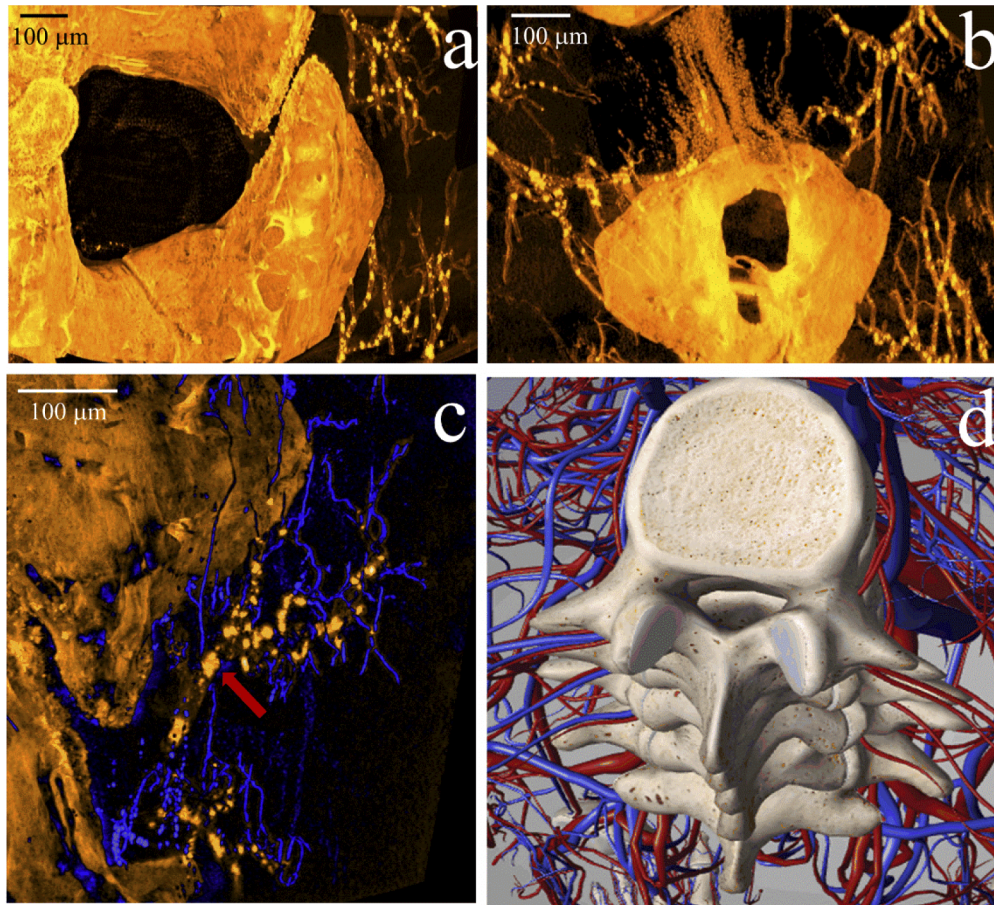

Fig. 5. (a), (b), (c) 3D view of the sample C (the cervical part) perfused with Microfil. The ascending vertebral arteries, partially filled, by the contrast are clearly seen, (c) the unstained small vasculature is virtually segmented and rendered in blue. (d) the sketch of the spine explains the orientation of the samples. (a-c) PSI TOMCAT beamline experiment. The images are obtained at incident energy 24 keV, pixel size of 1.6 micron and the sample-detector distance 0.21 m. The number of tomographic projections is equal to 1601.
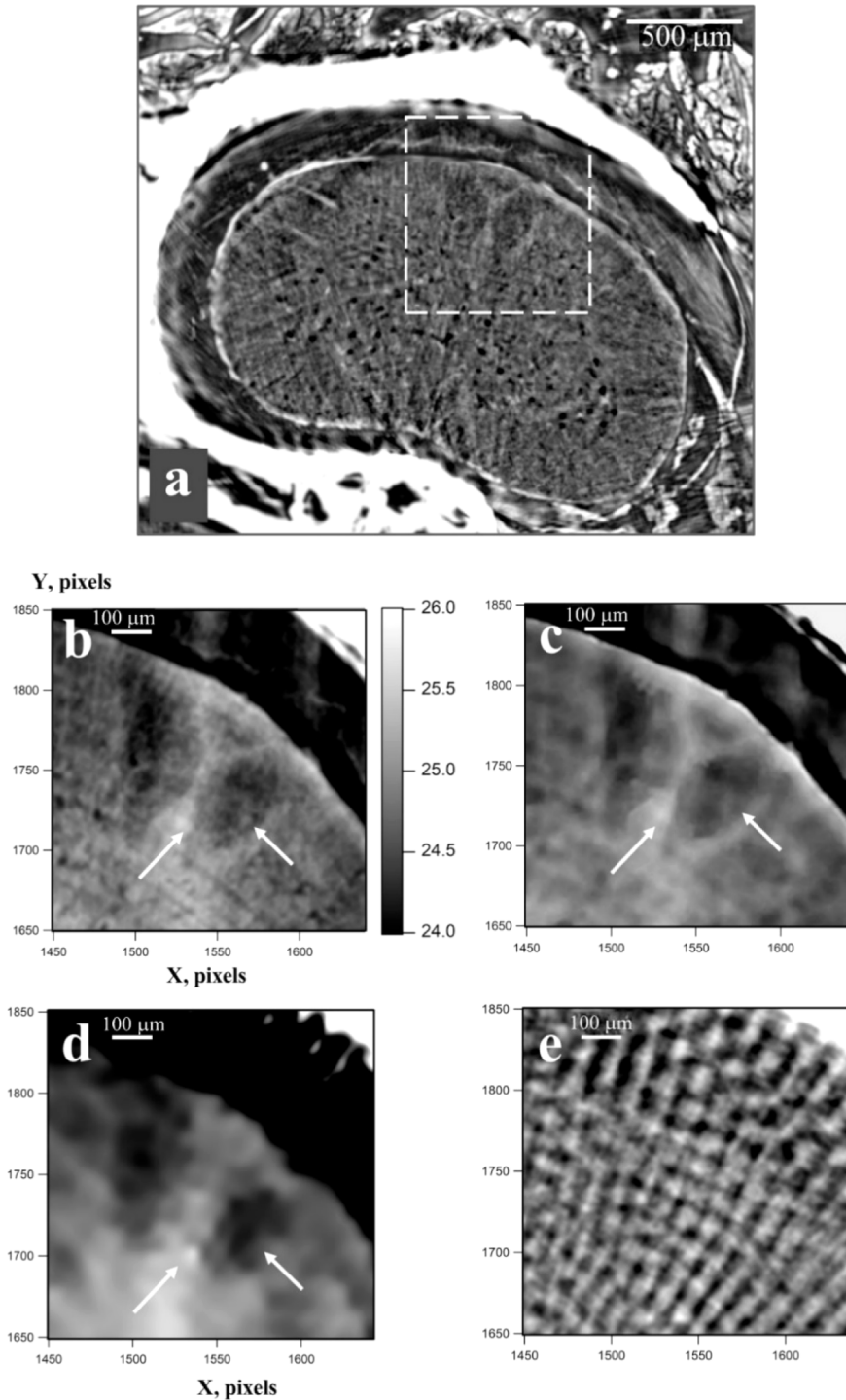
Fig. 6. (a) Single slice in the axial view of the sample A corresponding to Fig. 2, reconstructed with full data set of 2000 projections; b) the zoom of the area tagged in (a) with the rectangular frame; (c, d) application of RegSIRT with regularization (see Eq. (4)) with sparse data set: (c) 500 angular projections, (d) 100 angular projections; (e) FBP reconstruction with sparse data set of 100 angular projections. RegSIRT allows recovering the morphological information lost by FBP. Pixel size is 3.5 micron.

the low absorbing tissue of the blood vessels and the high absorbing contrast agent are clearly distinguished. The small vasculature, not filled by the stain, is well visible too; it is segmented and rendered in blue in Fig. 5(c). These results demonstrate that in micro-XPCT vessels are clearly visible without the need of contrast agent, which, when present, further enhances the contrast.

2.3. *Tomographic reconstruction with sparse data set*

In order to investigate the possibility of reducing the number of projections needed to reconstruct computed tomographic images maintaining a significant diagnostic level, we tested, in addition to FBP, also the RegSIRT iterative algorithm. Reconstructions in Fig. 6(c-e) were performed using the data set with evenly spaced omitted projections to reduce the number of projections. Figure 6(a) shows a single slice of the sample A (the cervical part of SP, axial view) in the same experimental conditions used for Fig. 2, reconstructed with the full data set of 2000 projections; in Fig. 6(a) we reported the results for FBP; RegSIRT gave an equivalent result (not shown). The zoom of the area tagged in Fig. 6(a) with the rectangular frame is shown in Fig. 6(b). Figures 6(c), and 6(d) show the results obtained using 50 iterations of RegSIRT with 500 and 100 projections, respectively. The RegSIRT reconstruction with sparse set of projections reported in Fig. 6(c,d) preserves morphological details of the SC. The FBP reconstruction with a sparse data set of 100 projections is reported in Fig. 6(e) showing a complete loss of information.

3. Discussion

The micro-XPCT in PBI geometry has enabled us to obtain detailed high spatial resolution 3D images of intact fixed post-mortem healthy murine spinal cord surrounded by vertebrae. The imaging technique used in our research does not require invasive preparations such as laminectomy (removal of the vertebral bone), sample drying, sectioning. We have shown that X-rays passing through the SC inside the spinal column preserve information about SC architecture at a multiscale level. Therefore, we were able to simultaneously characterize the three-dimensional morphology of the spinal cord at scales spanning from the whole organ to the vascular and neuronal organization. In the perspective of preparing the way to high resolution in-vivo neuroimaging, we have also shown that the application of advanced iterative tomographic reconstruction methods allows significantly reducing the number of tomographic projections.

The possibility to study the alterations of the CNS and in particular of the spinal cord without removing the vertebrae, in post-mortem and, in perspective, in-vivo experiments at high spatial resolution will be of fundamental importance in the development of effective therapies to alleviate pathological or traumatological effects of spinal cord injuries.

This work was performed on fixed SC tissues. Although fixation preserves the tissues, however, it may induce tissue alterations that significantly modify the SC morphology with respect to the in-vivo pattern. Before extending and generalizing the significance of these results further investigations with unfixed samples are therefore required.

Until now, high-resolution 3D X-ray imaging of the intact spine resulted to be a challenging task. In this work, we have evaluated different experimental conditions, i.e. different incident energies, sample-to-detector distances and spatial resolutions, to attain high-resolution, contrast agent-free 3D images of the intact SC in the spine canal.

In this regard, we have shown post-mortem experiments using 60 keV X-rays. The resulting images at a pixel size of about 3 micron show only the macroscopic morphological structure of the SC. As expected, by increasing the spatial resolution (pixel size of about 1 micron) and by injecting a contrast agent (Iodixanol) in the blood vessels of the sample B, the image of the vascularization network appeared, however micro-morphology of the soft tissue, in particular neuronal network, was indistinguishable.

By decreasing the X-ray energy down to 20-30 keV, even without any contrast agent and at low spatial resolution, the features comparable with the vascularization and neuron cells were visible; the visibility was further enhanced by using a higher spatial resolution (pixel size of about 1 micron). Finally, we can deduce that the contrast agent is not a necessary requirement for SC imaging with XPCT. Moreover, we can conclude that the incident energy plays an important role; lower incident monochromatic energy provides better SC visualization. However, we should highlight that, when in-vivo experiments will be considered, the trade-off between visibility of SC micro-morphology and absorbed dose in the sample have to be taken into consideration.

The spatial resolution is a fundamental parameter in spinal cord imaging; in the future perspective of in-vivo experiments, the pixel size should not be too small because this would determine an increased image acquisition time and accordingly, also the delivered dose. In general, the exposure time in our experiments has been optimized in order to obtain the best signal-to-noise ratio on a single projection. At this stage we did not care about the total time necessary to measure the whole region of interest, which is, however, still quite reasonable for standard post-mortem experiments (~5-10 min depending on the image and the energy used).

We have tested different algorithms to preserve the details visibility using a limited number of projections. In particular, we applied FBP and the RegSIRT algorithms. RegSIRT is based on a simultaneous algebraic approach, which is highly flexible to the specific problems: any prior information can be incorporated in the reconstruction model, providing better quality of 3D images with undersampled and/or noisy data. We applied the approach with independent phase retrieval and tomographic reconstruction steps. Generally, the phase retrieval process can be directly integrated into a tomographic reconstruction procedure [41,42], but, considering the complexity of the samples under investigation, we adopted a two-step reconstruction approach.

FBP provides fast and good quality image reconstruction – with high signal-to-noise ratio (SNR) – using projections acquired at a sufficiently large number of angles, evenly spaced over a 180 or 360 degrees rotation angle. However, FBP provides poor results and leads to image artifacts for undersampled and noisy data, which is typical in low-dose in-vivo imaging. The algebraic approach is one of the promising numerical techniques under development to solve this problem [34,43,44]. On the other hand, as an iterative method, SIRT is computationally expensive, which starts to be a bottleneck for its application in biomedicine. This problem has been alleviated by using the computer accelerator technology, and, in particular, the GPU-based High-Performance Computing. The computational time per single iteration of RegSIRT algorithm is comparable with that of an FBP reconstruction but the total computational time of RegSIRT increases as several iterations are needed to reach convergence. Results show a quite fast convergence of RegSIRT with 50 iterations. Thanks to modern parallel GPU architectures, a single iteration of RegSIRT require a few seconds to reconstruct a 2560 X 2560 pixels image. Thus a few minutes are required to reconstruct a single slice of the whole scanned volume. The total computational time for the reconstruction of the whole volume is basically dependent on the degree of parallelism offered by the available hardware.

In our paper we have shown that the RegSIRT allows reducing the number of projections by up to 20 times with respect to the original 2000 set; the same reduction applied to FBP leads instead to meaningless data. It should be noted that some regions of the sample in the regSIRT reconstruction look patchy and oversmoothed that worsen the final spatial resolution. Different strategies have been proposed to reduce the undesired artifacts in images with sparse projections, one of the most interesting and promising of them is super resolution technique [45].

The dose to the sample in XPCT imaging with 100 projections has been estimated using the data acquisition parameters and applying the algorithms reported in Ref. [46]. The dose is still a roughly a factor of 20 higher than that suited in longitudinal studies, however the steps made to allow the full visualization of intact samples, and the significant dose reduction possible

by acquiring data at a 20 times reduced projection number, represent important results in this perspective.

It has been shown in Refs. [47,48] that for a biological sample signal-to-noise ratio lowering per view impacts the conventional CT reconstruction less than artifacts due to the reduced sampling. This result requires further accurate experimental and quantitative study to approve it for in-vivo spinal cord XPCT imaging.

Another big challenge in the 3D visualization is the removal of artifacts generated by the strong absorbing areas of the sample or/and by a low dynamic range and resolution of the detector. This problem can be resolved only partially with pre-/post- processing procedures. In some areas of our samples the residual artifacts prevent the interpretation of the reconstructed image. The optimization of experimental parameters and further development of a computational platform to reduce the radiation dose and to minimize reconstruction artifacts are the next challenges to be dealt.

4. Material and methods

4.1. Sample preparation

All procedures involving animals and their care were conducted according to European Union (directive 2010/63/EU) and Italian (Decreto Legislativo n.26, 4 March 2014) laws and policies. The research protocol was approved by the Ethical Committee for Animal Experimentation of the University of Genoa (Prot. 319).

Adult male C57 Black mice (20–22 g, body weight) were purchased from Charles River, Calco, Italy and kept at 22°C and humidity of 40% on a 12-h light/dark cycle with food and water ad libitum. Mice were divided into three groups (A, B, C): Samples A were perfused with saline solution, while Samples B and Samples C were perfused with Iodixanol and Microfil, (Flow Tech, Inc., Carver, MA), respectively.

Samples A & C: were anesthetized by an intraperitoneal injection of ketamine (80 mg/kg)/xylazine (10 mg/kg) mixture and then perfused transcardially with saline solution containing heparin (50 U/ml) using a catheter inserted into the left ventricle connected to a pressure-controlled pump. The blood in the cerebral vessels was drained out through an incision on right atrium. Samples A, after flashing the blood, were perfused with 4% PFA in 0.1 M PBS (at room temperature) at 50 mmHg for 5 min at a filling rate of 2 mL/min. Samples C were perfused transcardially by Microfil.

After the perfusion, the intact mouse spine was extracted and placed in 4% PFA for 24h overnight at 4°C for the solidification process, and then maintained in 70% ethanol [49].

Sample B: was anesthetized using solution of ketamine (80-100 mg/kg)/xylazine (10-12.5 mg/kg), administered by intraperitoneal injection. The perfusion system was prepared as follows: a medium-small diameter needle was connected to a small-diameter tube carrying the perfusion fluids, the other tube end being immersed in the flask of filtered, degassed heparinized saline connected to a peristaltic pump. We pushed off all the air bubbles remaining in the tube by acting on the pump, while discharging the accompanying liquids into a discard beaker until a continuous liquid flux was detectable at sight. With the pump switched-off, the liquid-filled needle was inserted into the left ventricle of the animal. By switching-on the pump, the solution was pushed into the circulatory system, washed out through a hole made in the right atrium. All the blood was progressively pushed off by the saline solution that was continuously circulated into the circulatory system (up to 70-80 cc) for some 10/15 minutes to clean thoroughly all the vessels. After, the peristaltic pump was turned off in order to substitute the heparinized saline solution with the tissue fixing 10% formalin solution (70-80 cc). The Iodixanol was then infused at the completion of the operations, the pump was turned off and the needle was extracted from the ventricle. 48 hours after the tissue fixation, the SCs were extracted and then immersed in PBS.

4.2. XPCT set-up

XPCT measurements were performed using the PBI set up [50] after having fixed the samples on a suitable holder to avoid samples movement during the acquisition.

Samples A and B were measured at the ID17 beamline (ESRF) with a monochromatic incident beam of 30 keV (sample A) and 60 keV (sample A&B), see Table 1. The tomography was acquired with 2000 projections and an exposure time of 0.4s for each projection covering a total angle range of 180 degrees.

Sample A was positioned at 2.3 m from the imaging system having a pixel size of 3.5 micron. The tomographic images of Sample B, on the other hand, were acquired using the 3.5 micron and 1-micron pixel size detectors placed at 2.3 m and 0.60 m from the sample, respectively

In addition, we measured the samples A & C at the TOMCAT beamline (SLS, Switzerland) using a monochromatic X-ray beam of 24 keV. An imaging system connected with a PCO.5.5 camera with a pixel size of 1.6 and 0.64 micron was set at 0.21 m and 0.05 m from the sample, respectively. The tomography has been acquired with 1601 projections (with exposure time of 0.2 s for each projection) covering a total angle range of 180 degrees. Sample C was measured using a pixel size of 1.6 micron, while sample A with pixel size of 1.6 micron and 0.64 micron (see Table 1).

4.3. Detectors and optics

ESRF: The detection system was composed by a YAG-based scintillator screen coupled with a visible-light optics and a PCO.Edge5.5 sCMOS detector (2560×2160 pixels) [51]. The study was carried out using both 2x and 10x optical magnification systems to determine a final pixel size of 3.5 and 1.0 micron, respectively (FOV: 8.9×7.5 mm^2 and 1.8×1.5 mm^2).

PSI: The detection system was composed of a LAG:Ce scintillators (20 μm thick) coupled with a PCO.Edge 5.5 (sCMOS-technology, 2560×2160 pixels, 6.5μm pixel size and a 16-bit nominal dynamic range) and microscope system based on diffraction-limited optics. The study was carried out using both 4x and 10x optical magnification systems to determine a final pixel size of 1.6 and 0.64 micron, respectively (FOV: 4.2×3.5 mm^2 & 1.7×1.4 mm^2).

4.4. Histology

After the measurements, spinal cord samples were first sectioned into cervical, thoracic, and lumbar parts. Then, each part was first dehydrated through a series of graded ethanol baths to remove the water, and then infiltrated with paraffin wax, and embedded into wax blocks. Samples were cut in a sliding microtome at 10 μm-thick sections in the axial plane, and six series of sections were collected. After paraffin removal, the first series of sections were stained with thionin (Nissl) to identify the cytoarchitectonic boundaries of various areas in the spinal cord. Nissl-stained sections were examined at 5x and 10x magnification in brightfield in a light microscope (Leica DMRB, Wetzlar, Germany). Additionally, sections were studied under darkfield to increase the contrast of boundaries between white and grey matter, and non-stained structures, such as blood vessels in the same microscope. Photomicrographs of cervical part of the spinal cord were taken with a digital camera attached to the microscope (DXM1200F, Nikon Instruments Inc., Japan).

4.5. Data processing

Data processing procedures include: pre-processing of the detected images, phase retrieval and tomographic reconstruction and post-processing of the reconstructed data.

The pre-processing included raw data flat- /dark-field correction and normalization with the average value of background outside the object and ring artefact reduction.

Phase contrast retrieval algorithm is based on the solution of the transport of intensity equation in the near field for paraxial monochromatic wave. It assumes that the object is composed of one or two distinct quasi homogeneous materials (bone and spinal cord tissue in our case). The logarithm of the retrieved intensity is calculated from the intensity $I(r_\perp, z = d)$ measured at the detector plane $z = \text{d}$, according to Refs. [29,32,33]:

$$T = \int \mu(r)dz = -\log_e \left(F_\perp^{-1} \frac{1}{1 + p^2 u^2} \left\{ F_\perp \left\{ \frac{I(r_\perp, z = d)}{I_0} \right\} \right\} \right) \tag{1}$$

where I_0 is the incident beam intensity, $r_\perp$ are lateral coordinates perpendicular to the optical axis z, u is spatial frequency reciprocal to $r_\perp$, and $F_\perp$ and $F_\perp^{-1}$ respectively are the two-dimensional forward and the inverse lateral Fourier transforms. We introduced the parameter $p^2 = 4\pi^2 d\Delta\delta/\Delta\mu$, where $\Delta\delta/\Delta\mu$ is the ratio of the differences in decrements $\Delta\delta = (\delta_1 - \delta_2)$ and in the linear attenuation indexes $\Delta\mu = (\mu_1 - \mu_2)$ of two adjoining materials with indexes 1 and 2 correspondingly. The phase retrieval algorithm valid in the high energy range 60-500 keV can be found in Ref. [52].

After retrieval procedure Eq. (1) at each projection angle, the resulting set of data is combined to reconstruct the 3D volume of the object.

After tomographic reconstruction, the post processing procedure has been applied to enhance visibility of the spinal cord inside of vertebrae. Standard tools and plugins of open source image program ImageJ/Fiji were used [40]. In particular, average intensity and maximum intensity projection options of the standard tool "Z Project" of ImageJ/Fiji were used.

The regSIRT algorithm was adopted for volume reconstruction with sparse set of projections.

In the algebraic approach, the inverse tomography problem reduces to a solution of a linear system of equations:

$$A\mu = T \tag{2}$$

where A is projection matrix accounting for the geometry of the tomographic system including pixel weights, vector μ is the object function that gives the spatial distribution of the reconstructed value (see Eq. (1)). T is the image vector given by the retrieved images at the object plane Eq. (1). Generally, the solution of Eq. (2) reduces to the solution of a minimization problem written in the form:

$$\frac{1}{2}\|A\mu - T\|^2 \to \min_\mu \tag{3}$$

We used Total variation regularization [36] to increase the extension of piece-wise smooth zones while their number decreases:

$$\frac{1}{2}\|A\mu - T\|^2 + \alpha\|\nabla\mu\|_1 \to \min_\mu, \tag{4}$$

where $\alpha > 0$ is a regularization parameter, that controls the influence of the regularization process on the final result. We applied the conjugated gradient method to solve the optimization problem [53]. The gradient $\nabla\mu$ computed with the finite difference method was optimized in the central node of each 9 neighbour-nodes patch and includes only the direct orthogonal neighbours.

4.6. Convergent rate of the regSIRT algorithm

We carried out a computer experiment based on the data obtained by measuring an unstained most-mortem mouse spinal cord with spine using XPCT technique at the biomedical beamline ID17 of the ESRF. During tomographic scanning a set of images is taken at different illumination angles evenly spaced over a 180 degrees rotation angle (the total number of projections was 2000), sample-to-detector distance was 2.3 m, energy of X-ray radiation was 30 keV, exposure time was 0.4 s for each projection. After a phase retrieval procedure, we reconstructed 3D image of the sample with a conventional non-iterative algorithm FBP and with the iterative algorithm

regSIRT. We applied both FBP and regSIRT algorithms to the full angular projections set with 2000 projections and to the sparse angle set with 50, 100, 200, 500, 1000 projections evenly spaced over a 180 degrees rotation angle. We estimated the convergent rate of RegSIRT algorithm with different number of sparse projections.

The convergent rate was calculated using two approaches.

First approach. Residual error after k iterations was calculated with the following equation:

$$Err_k = \sum_{\text{for pixel in object}} (\mu_k - \mu_{k-1})^2 , \tag{5}$$

where μ_k is the reconstruction result after κ iterations, μ_{k-1} is the reconstruction result after the $(\kappa-1)$ iterations.

Second approach. Error after k iterations was calculated with the following equation:

$$Err_k = \sum_{\text{for pixel in sinogram space}} (A\mu_k - T)^2 \tag{6}$$

where A is corresponding element of projection matrix accounting for the geometry of the tomographic system including pixel weights, μ_k is the reconstruction result after k iterations, T is logarithm of the correspondent element of the retrieved image (see Eq. (1)).

The convergent rate graphs computed with Eq. (5) in the RegSIRT experiment with 50 and 100 projections are presented in Fig. 7(a,b) on a linear scale. The logarithm of the error computed with Eq. (5) and Eq. (6) in RegSIRT reconstruction with 50, 100, 200, 500, 1000 projections is shown in Fig. 8 as graphs on a semilogarithmic scale. Convergence rate graphs presented in Fig. 7 and Fig. 8 show that 50 iterations are a reasonable value for the convergence of RegSIRT reconstruction procedure.

As a next step we used 50 iterations of RegSIRT algorithm to reconstruct 3D image of the sample with different number of projections and we compared these images with FBP algorithm reconstructions. We found that RegSIRT for the selected sample provides qualitatively better result compare with FBP for projections number less than 500. Tomographic reconstructions of the sample obtained with FBP (2000 and 100 projections) and with regSIRT algorithm (100 and 500 projections) are shown in Fig. 6.
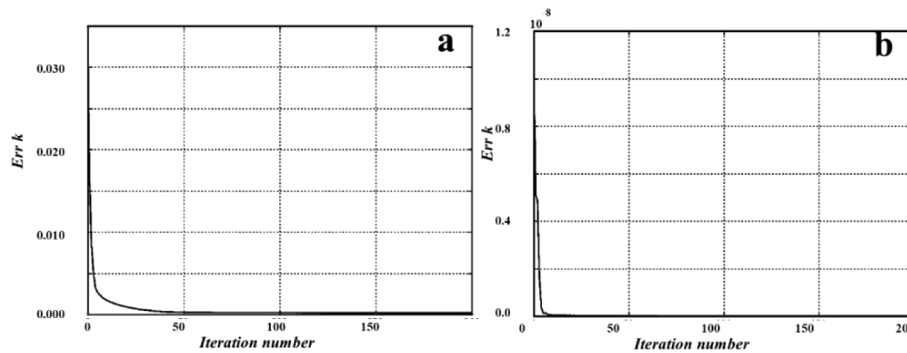

Fig. 7. Convergent rate computed with Eq. (5) in the RegSIRT experiment with (a) 50 and (b) 100 projections.

4.7. Computational platform

Data pre-processing, artefact removal, phase retrieval and FBP reconstruction were done with the open-source software toolkit SYRMEP Tomo Project (STP) [54,55].
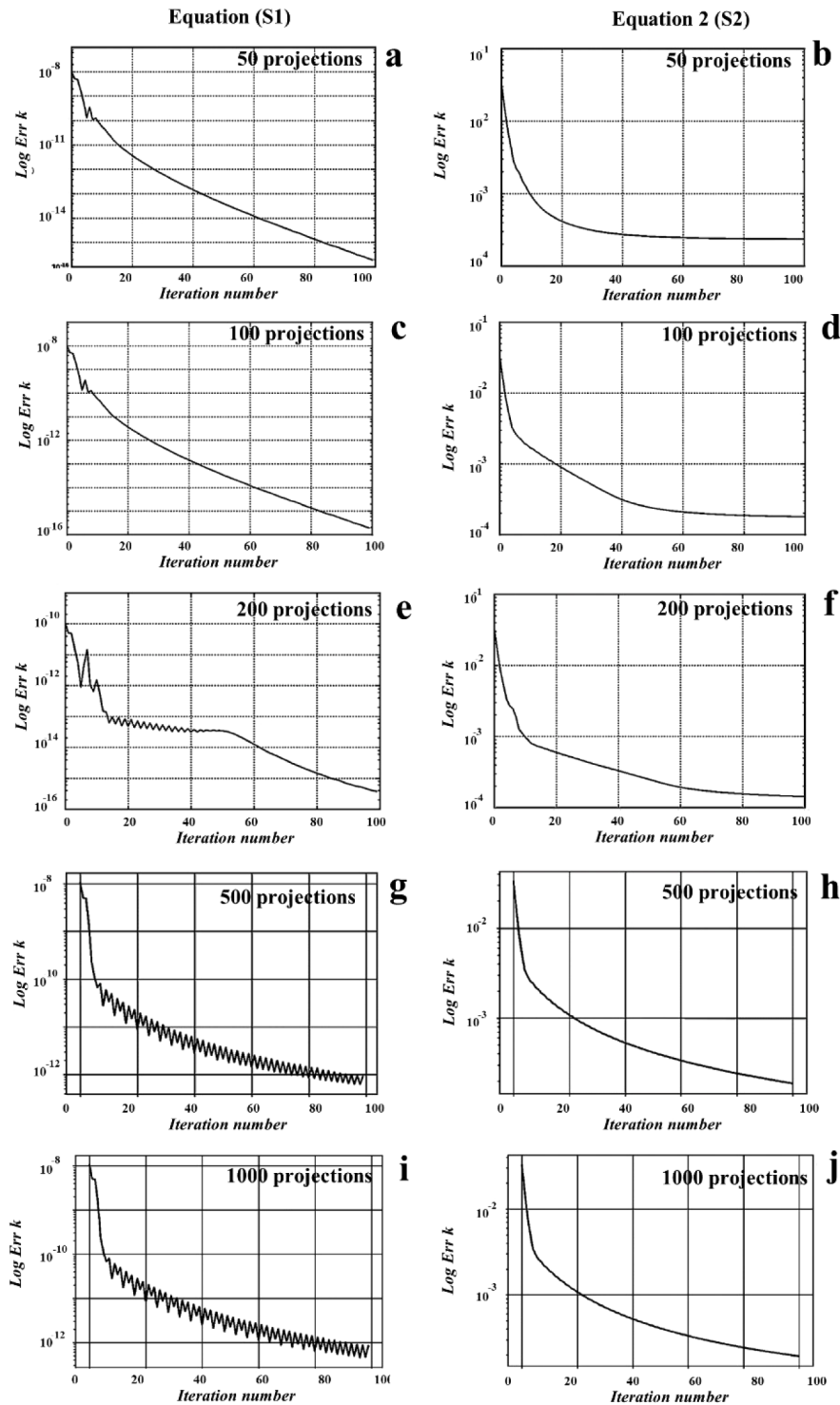
Fig. 8. Convergence rate graphs of regSIRT algorithm on a semilogarithmic scale. Graphs at the left column are calculated with Eq. (5), graphs at the right column is calculated with Eq. (6); (a, b) 50 projections; (c, d) 100 projections; (e, f) 200 projections; (g, h) 500 projections ; (i, j) 1000 projections.

RegSIRT reconstruction were done with software developed by Shubnikov Institute of Crystallography (Moscow, Russia) [38,39]. ASTRA toolbox was applied for GPU-accelerated computation of forwards/backwards operations in tomographic reconstruction [56].

Post-processing and 3D rendering procedures were done using image processing program Fiji /ImageJ [40]. Function "Intensity Z-projection" (ImageJ/Fiji) allows the 3-D dataset to be visualized in 2-D. It is useful to highlight specific details from the stack. Both maximum and average z-projections have been used for the comparison with the histology, which is a 2D technique and the information in depth is averaged within 10 microns.

Funding

Acknowledgements

Disclosures

The authors declare no competing financial and/or non-financial interests.

References

1. N. Hasnan, "International Perspectives on Spinal Cord Injury," (2013).
2. M. Soubeyrand, A. Badner, R. Vawda, Y. S. Chung, and M. G. Fehlings, "Very high resolution ultrasound imaging for real-time quantitative visualization of vascular disruption after spinal cord injury," J. Neurotrauma **31**(21), 1767–1775 (2014).
3. M. J. Farrar, I. M. Bernstein, D. H. Schlafer, T. A. Cleland, J. R. Fetcho, and C. B. Schaffer, "Chronic in vivo imaging in the mouse spinal cord using an implanted chamber," Nat. Methods **9**(3), 297–302 (2012).
4. A. Ertürk, C. P. Mauch, F. Hellal, F. Förstner, T. Keck, K. Becker, N. Jährling, H. Steffens, M. Richter, M. Hübener, E. Kramer, F. Kirchhoff, H. U. Dodt, and F. Bradke, "Three-dimensional imaging of the unsectioned adult spinal cord to assess axon regeneration and glial responses after injury," Nat. Med. **18**(1), 166–171 (2012).
5. G. J. Cowin, T. J. Butler, N. D. Kurniawan, C. Watson, and R. H. Wallace, "Magnetic resonance microimaging of the spinal cord in the SOD1 mouse model of amyotrophic lateral sclerosis detects motor nerve root degeneration," NeuroImage **58**(1), 69–74 (2011).
6. P. Glover and S. P. Mansfield, "Limits to magnetic resonance microscopy," Rep. Prog. Phys. **65**(10), 1489–1511 (2002).

7. J. Dudak, J. Zemlicka, J. Karch, M. Patzelt, J. Mrzilkova, P. Zach, Z. Hermanova, J. Kvacek, and F. Krejci, "High-contrast X-ray micro-radiography and micro-CT of ex-vivo soft tissue murine organs utilizing ethanol fixation and large area photon-counting detector," Sci. Rep. **6**(1), 30385 (2016).

8. C. L. Gregg, A. K. Recknagel, and J. T. Butcher, "Micro/Nano-Computed Tomography Technology for Quantitative Dynamic, Multi-scale Imaging of Morphogenesis," Methods Mol. Biol. **1189**, 47–61 (2015).

9. M. Kampschulte, A. C. Langheinirch, J. Sender, H. D. Litzlbauer, U. Althöhn, J. D. Schwab, E. Alejandre-Lafont, G. Martels, and G. A. Krombach, "Nano-Computed Tomography: Technique and Applications," Rofo-fortschritte Auf Dem Gebiet Der Rontgenstrahlen Und Der Bildgeb. Verfahren **188**(02), 146–154 (2016).

10. R. Mizutani and Y. Suzuki, "X-ray microtomography in biology," Micron **43**(2-3), 104–115 (2012).

11. P. L. Salmon and A. Y. Sasov, "Application of Nano-CT and High-Resolution Micro-CT to Study Bone Quality and Ultrastructure, Scaffold Biomaterials and Vascular Networks," 323–331 (2007).

12. D. P. Clark and C. T. Badea, "Micro-CT of rodents: state-of-the-art and future perspectives," Phys. Medica **30**(6), 619–634 (2014).

13. R. Müller, "Hierarchical microimaging of bone structure and function," Nat. Rev. Rheumatol. **5**(7), 373–381 (2009).

14. B. D. Metscher, "MicroCT for comparative morphology: simple staining methods allow high-contrast 3D imaging of diverse non-mineralized animal tissues," BMC Physiol. **9**(1), 11 (2009).

15. J. M. de S. e Silva, I. Zanette, P. B. Noël, M. B. Cardoso, M. A. Kimm, and F. Pfeiffer, "Three-dimensional non-destructive soft-tissue visualization with X-ray staining micro-tomography," Sci. Rep. **5**(1), 14088 (2015).

16. S. Heinzer, G. Kuhn, T. Krucker, E. P. Meyer, A. Ulmann-Schuler, M. Stampanoni, M. Gassmann, H. H. Marti, R. Müller, and J. Vogel, "Novel three-dimensional analysis tool for vascular trees indicates complete micro-networks, not single capillaries, as the angiogenic endpoint in mice overexpressing human VEGF(165) in the brain," NeuroImage **39**(4), 1549–1558 (2008).

17. J. Hu, Y. Cao, T. Wu, D. Li, and H. Lu, "High-resolution three-dimensional visualization of the rat spinal cord microvasculature by synchrotron radiation micro-CT," Med. Phys. **41**(10), 101904 (2014).

18. D. Chapman, W. Thomlinson, R. E. Johnston, D. Washburn, E. Pisano, N. Gmür, Z. Zhong, R. Menk, F. Arfelli, and D. Sayers, "Diffraction enhanced x-ray imaging," Phys. Med. Biol. **42**(11), 2015–2025 (1997).

19. A. Snigirev, I. Snigireva, V. Kohn, S. Kuznetsov, and I. Schelokov, "On the possibilities of x-ray phase contrast microimaging by coherent high-energy synchrotron radiation," Rev. Sci. Instrum. **66**(12), 5486–5492 (1995).

20. S. W. Wilkins, T. E. Gureyev, D. Gao, A. Pogany, and A. W. Stevenson, "Phase-contrast imaging using polychromatic hard X-rays," Nature **384**(6607), 335–338 (1996).

21. A. Momose, T. Takeda, Y. Itai, and K. Hirano, "Phase-contrast X-ray computed tomography for observing biological soft tissues," Nat. Med. **2**(4), 473–475 (1996).

22. C. David, B. Nöhammer, H. H. Solak, and E. Ziegler, "Differential x-ray phase contrast imaging using a shearing interferometer," Appl. Phys. Lett. **81**(17), 3287–3289 (2002).

23. A. Olivo, F. Arfelli, G. Cantatore, R. Longo, R. H. Menk, S. Pani, M. Prest, P. Poropat, L. Rigon, G. Tromba, E. Vallazza, and E. Castelli, "An innovative digital imaging set-up allowing a low-dose approach to phase contrast applications in the medical field," Med. Phys. **28**(8), 1610–1619 (2001).

24. D. M. Connor, H. Benveniste, F. A. Dilmanian, M. F. Kritzer, L. M. Miller, and Z. Zhong, "Computed tomography of amyloid plaques in a mouse model of Alzheimer's disease using diffraction enhanced imaging," NeuroImage **46**(4), 908–914 (2009).

25. M. Fratini, I. Bukreeva, G. Campi, F. Brun, G. Tromba, P. Modregger, D. Bucci, G. Battaglia, R. Spanò, M. Mastrogiacomo, H. Requardt, F. Giove, A. Bravin, and A. Cedola, "Simultaneous submicrometric 3D imaging of the micro-vascular network and the neuronal system in a mouse spinal cord," Sci. Rep. **5**(1), 8514 (2015).

26. I. Bukreeva, G. Campi, M. Fratini, R. Spanò, D. Bucci, G. Battaglia, F. Giove, A. Bravin, A. Uccelli, C. Venturi, M. Mastrogiacomo, and A. Cedola, "Quantitative 3D investigation of Neuronal network in mouse spinal cord model," Sci. Rep. **7**(1), 41054 (2017).

27. N. M. Das, S. Hatsell, K. Nannuru, L. Huang, X. Wen, L. Wang, L.-H. Wang, V. Idone, J. A. Meganck, A. Murphy, A. Economides, and L. Xie, "In Vivo Quantitative Microcomputed Tomographic Analysis of Vasculature and Organs in a Normal and Diseased Mouse Model," PLoS One **11**(2), e0150085 (2016).

28. Z. Starosolski, C. A. Villamizar, D. Rendon, M. J. Paldino, D. M. Milewicz, K. B. Ghaghada, and A. V. Annapragada, "Ultra High-Resolution In vivo Computed Tomography Imaging of Mouse Cerebrovasculature Using a Long Circulating Blood Pool Contrast Agent," Sci. Rep. **5**(1), 10178 (2015).

29. D. Paganin, S. C. Mayo, T. E. Gureyev, P. R. Miller, and S. W. Wilkins, "Simultaneous phase and amplitude extraction from a single defocused image of a homogeneous object," J. Microsc. **206**(1), 33–40 (2002).

30. M. A. Beltran, D. Paganin, K. Uesugi, and M. J. Kitchen, "2D and 3D X-ray phase retrieval of multi-material objects using a single defocus distance," Opt. Express **18**(7), 6423–6436 (2010).

31. M. Beltran, D. Paganin, K. Siu, A. Fouras, S. Hooper, D. Reser, and M. Kitchen, "Interface-specific x-ray phase retrieval tomography of complex biological organs," Phys. Med. Biol. **56**(23), 7353–7369 (2011).

32. M. Ullherr and S. Zabler, "Correcting multi material artifacts from single material phase retrieved holo-tomograms with a simple 3D Fourier method," Opt. Express **23**(25), 32718–32727 (2015).

33. L. C. P. Croton, K. S. Morgan, D. M. Paganin, L. T. Kerr, M. J. Wallace, K. J. Crossley, S. L. Miller, N. Yagi, K. Uesugi, S. B. Hooper, and M. J. Kitchen, "In situ phase contrast X-ray brain CT," Sci. Rep. **8**(1), 11412 (2018).

34. P. Gilbert, "Iterative methods for the three-dimensional reconstruction of an object from projections," J. Theor. Biol. **36**(1), 105–117 (1972).

35. A. C. Kak, M. Slaney, and G. Wang, *Principles of Computerized Tomographic Imaging* (1988).

36. A. Chambolle, V. Caselles, M. Novaga, D. Cremers, and T. Pock, "An introduction to Total Variation for Image Analysis," **9**, 263–340 (2009).

37. V. V. Estrela, H. A. Magalhães, and O. Saotome, "Total Variation Applications in Computer Vision," arXiv Prepr. arXiv1603.09599 543–570 (2016).

38. A. Buzmakov, D. Nikolaev, M. Chukalina, and G. Schaefer, "Efficient and effective regularised ART for computed tomography," in *2011 Annual International Conference of the IEEE Engineering in Medicine and Biology Society* (2011), Vol. 2011, pp. 6200–6203.

39. M. V. Chukalina, A. S. Ingacheva, A. V. Buzmakov, Y. S. Krivonosov, V. E. Asadchikov, and D. P. Nikolaev, "A Hardware and Software System for Tomographic Research: Reconstruction via Regularization," Bull. Russ. Acad. Sci.: Phys. **83**(2), 150–154 (2019).

40. J. Schindelin, I. Arganda-Carreras, E. Frise, V. Kaynig, M. Longair, T. Pietzsch, S. Preibisch, C. T. Rueden, S. Saalfeld, B. Schmid, J.-Y. Tinevez, D. J. White, V. Hartenstein, K. Eliceiri, P. Tomancak, and A. Cardona, "Fiji: an open-source platform for biological-image analysis," Nat. Methods **9**(7), 676–682 (2012).

41. A. V. Bronnikov, "Reconstruction formulas in phase-contrast tomography," Opt. Commun. **171**(4-6), 239–244 (1999).

42. L. Hehn, K. Morgan, P. Bidola, W. Noichl, R. Gradl, M. Dierolf, P. B. Noël, and F. Pfeiffer, "Nonlinear statistical iterative reconstruction for propagation-based phase-contrast tomography," APL Bioeng. **2**(1), 016105 (2018).

43. D. Chen, B. Goris, F. Bleichrodt, H. H. Mezerji, S. Bals, K. J. Batenburg, and H. Friedrich, "The properties of SIRT, TVM, and DART for 3D imaging of tubular domains in nanocomposite thin-films and sections," Ultramicroscopy **147**, 137–148 (2014).

44. J. Gregor and T. Benson, "Computational Analysis and Improvement of SIRT," IEEE Trans. Med. Imaging **27**(7), 918–924 (2008).

45. G. Zang, M. Aly, R. Idoughi, P. Wonka, and W. Heidrich, "Super-Resolution and Sparse View CT Reconstruction," in *Proceedings of the European Conference on Computer Vision (ECCV)* (2018), pp. 145–161.

46. A. Mittone, F. Baldacci, A. Bravin, E. Brun, F. Delaire, C. Ferrero, S. Gasilov, N. Freud, J. M. Létang, D. Sarrut, F. Smekens, and P. Coan, "An efficient numerical tool for dose deposition prediction applied to synchrotron medical imaging and radiation therapy," J. Synchrotron Radiat. **20**(5), 785–792 (2013).

47. M. J. Kitchen, G. A. Buckley, T. E. Gureyev, M. J. Wallace, N. Andres-Thio, K. Uesugi, N. Yagi, and S. B. Hooper, "CT dose reduction factors in the thousands using X-ray phase contrast," Sci. Rep. **7**(1), 15953 (2017).

48. P. C. Hansen and J. H. Jørgensen, "Total Variation and Tomographic Imaging from Projections," *36th Conf. Dutch-Flemish Numer. Anal. Communities Woudschouten* (2011).

49. E. Stefanutti, A. Sierra, P. Miocchi, L. Massimi, F. Brun, L. Maugeri, I. Bukreeva, A. Nurmi, G. B. Provinciali, G. Tromba, O. Gröhn, F. Giove, A. Cedola, and M. Fratini, "Assessment of the effects of different sample perfusion procedures on phase-contrast tomographic images of mouse spinal cord," J. Instrum. **13**(03), C03027 (2018).

50. A. Bravin, P. Coan, and P. Suortti, "X-ray phase-contrast imaging: from pre-clinical applications towards clinics," Phys. Med. Biol. **58**(1), R1–R35 (2013).

51. A. Mittone, I. Manakov, L. Broche, C. Jarnias, P. Coan, and A. Bravin, "Characterization of a sCMOS-based high-resolution imaging system," J. Synchrotron Radiat. **24**(6), 1226–1236 (2017).

52. X. Wu, H. Liu, and A. Yan, "X-ray phase-attenuation duality and phase retrieval," Opt. Lett. **30**(4), 379–381 (2005).

53. J. Nocedal and S. J. Wright, *Numerical Optimization (Springer Series in Operations Research and Financial Engineering)* (Springer, 2000).

54. F. Brun, L. Massimi, M. Fratini, D. Dreossi, F. Billé, A. Accardo, R. Pugliese, and A. Cedola, "SYRMEP Tomo Project: a graphical user interface for customizing CT reconstruction workflows," Adv. Struct. Chem. Imaging **3**(1), 4 (2017).

55. L. Massimi, F. Brun, M. Fratini, I. Bukreeva, and A. Cedola, "An improved ring removal procedure for in-line x-ray phase contrast tomography," Phys. Med. Biol. **63**(4), 045007 (2018).

56. W. van Aarle, W. J. Palenstijn, J. De Beenhouwer, T. Altantzis, S. Bals, K. J. Batenburg, and J. Sijbers, "The ASTRA Toolbox: A platform for advanced algorithm development in electron tomography," Ultramicroscopy **157**, 35–47 (2015).